Published in final edited form as:
Phys Med Biol. 2009 April 21; 54(8): 2359–2376. doi:10.1088/0031-9155/54/8/007.

NEMA NU 2-2007 performance measurements of the Siemens Inveon™ preclinical small animal PET system

Brad J Kemp[1,3], **Carrie B Hruska**[1], **Aaron R McFarland**[2], **Mark W Lenox**[2], and **Val J Lowe**[1]

[1] Department of Radiology, Mayo Clinic, Rochester, MN, USA

[2] Preclinical Collaborations, Siemens Medical Solutions, Knoxville, TN, USA

Abstract

National Electrical Manufacturers Association (NEMA) NU 2-2007 performance measurements were conducted on the Inveon™ preclinical small animal PET system developed by Siemens Medical Solutions. The scanner uses 1.51 × 1.51 × 10 mm LSO crystals grouped in 20 × 20 blocks; a tapered light guide couples the LSO crystals of a block to a position-sensitive photomultiplier tube. There are 80 rings with 320 crystals per ring and the ring diameter is 161 mm. The transaxial and axial fields of view (FOVs) are 100 and 127 mm, respectively. The scanner can be docked to a CT scanner; the performance characteristics of the CT component are not included herein. Performance measurements of spatial resolution, sensitivity, scatter fraction and count rate performance were obtained for different energy windows and coincidence timing window widths. For brevity, the results described here are for an energy window of 350–650 keV and a coincidence timing window of 3.43 ns. The spatial resolution at the center of the transaxial and axial FOVs was 1.56, 1.62 and 2.12 mm in the tangential, radial and axial directions, respectively, and the system sensitivity was 36.2 cps kBq^{-1} for a line source (7.2% for a point source). For mouse- and rat-sized phantoms, the scatter fraction was 5.7% and 14.6%, respectively. The peak noise equivalent count rate with a noisy randoms estimate was 1475 kcps at 130 MBq for the mouse-sized phantom and 583 kcps at 74 MBq for the rat-sized phantom. The performance measurements indicate that the Inveon™ PET scanner is a high-resolution tomograph with excellent sensitivity that is capable of imaging at a high count rate.

Introduction

Preclinical small animal positron emission tomography (PET) is an essential tool in translational research areas such as gene expression and pharmaceutical development (Herschman 2003, Cherry 2006). PET imaging of picomolar concentrations of radiopharmaceuticals in animal models permit the spatial and temporal *in vivo* measurement of biological processes. Since PET is a non-invasive imaging technique, an animal can be imaged repeatedly and therefore an animal can serve as its own control; this minimizes the effects of inter-animal variability and thus the number of animals required to obtain statistically reliable data (Hume *et al* 1997). Clinical PET systems designed to image humans have a limited role in preclinical PET imaging as they lack the performance specifications necessary for imaging small animal models (Tatsumi *et al* 2003). The small anatomic structures of rodent models require that the spatial resolution of a preclinical PET scanner be greater than that of a clinical scanner for accurate quantification of the radiopharmaceutical distribution. Moreover, the sensitivity of a preclinical PET scanner is also important, as the activity and

[3]Author to whom any correspondence should be addressed: kemp.brad@mayo.edu.

volume of the injected tracer must be limited due to radiation dosimetry (Funk *et al* 2004) and mass-effect considerations, respectively (Hume *et al* 1998).

To this end, a variety of dedicated preclinical PET systems have been designed (Lecomte *et al* 1994, Cherry *et al* 1997, Jeavons *et al* 1999, Tai *et al* 2005, Huisman *et al* 2007, Laforest *et al* 2007, Kim *et al* 2007). One such preclinical system is the Siemens Inveon™ PET scanner (Siemens Medical Solutions, Knoxville, TN). This scanner is the successor to the Focus 120 PET scanner (Laforest *et al* 2007, Kim *et al* 2007). The design objectives for the Inveon™ were twofold: to produce a scanner with higher sensitivity yet similar resolution characteristics to the Focus 120 PET scanner, and to develop an extensible, high-speed electronics architecture for preclinical PET that is readily adaptable to multi-modality imaging.

To improve the system sensitivity, the solid angle subtended by the detector system was increased by extending the axial field of view from 76 mm to 127 mm; this also means that a whole-body scan of a mouse can be performed in a single bed position. However, with the greater solid angle, there is a definite possibility that more activity will be in the scanner during an imaging session. Therefore, the front-end and coincidence detection electronics must have sufficient count rate capability to minimize deadtime and pulse-pileup. The Inveon™ PET system employs new high-speed architecture, called Quicksilver, to meet this requirement (Newport *et al* 2006).

The purpose of this study is to report the performance characteristics of the Inveon™ PET scanner. The National Electrical Manufacturers Association (NEMA) NU 2-2007 performance standard was modified to measure the imaging characteristics of this small animal PET system.

Materials and methods

PET system design

The Inveon™ PET scanner uses lutetium oxyorthosilicate (LSO) crystals of dimensions 1.51 × 1.51 × 10 mm in the tangential, axial and radial directions, respectively. The crystal pitch is 1.63 mm and 1.59 mm in transaxial and axial directions, respectively, and the packing fraction is 92%. The LSO crystals are grouped into 20 × 20 blocks and each block is coupled to a Hamamatsu C-12 position-sensitive photomultiplier tube (PMT) using tapered light guides. Four blocks are arranged axially into a module; there are 16 modules in the system that define 80 rings with 320 crystals per ring. The ring diameter is 161 mm and the transaxial and axial FOVs are 100 mm and 127 mm, respectively. The transaxial bore size is 120 mm.

The Inveon™ PET system uses the Quicksilver asynchronous event processing architecture (Newport *et al* 2006). An Event Processing Module (EPM) is interfaced to each PMT; there are 16 EPMs in the system arranged in a ring configuration. The EPM digitizes the signal from the PMT and processes the signals for spatial position, energy and time. The EPM stores the events locally and then passes the digitized event to other EPMs, with communication and data transfer between EPMs based on a ‘store-and-forward’ concept to the nearest neighbors. The ‘store-and-forward’ concept enables the coincidence determination to be performed within the EPMs as the data from other EPMs pass through them, thereby distributing coincidence determination from one coincidence processor to 16 coincidence processors. There are eight high-speed digital channels between EPMs operating at 2.0 Gbits s^{-1} each, yielding an effective bandwidth between EPMs of 16 Gbits s^{-1}. The EPMs operate on a major clock cycle of 128 ns and each EPM can potentially transmit up to 15.6M energy and position qualified single events per second (Atkins *et al* 2006). The data packets are also routed through the Event Routing Subsystem (ERS) which acts as the data transport interface between the EPMs and the acquisition workstation (McFarland *et al* 2006). The ERS has two transport interfaces for

acquiring events: an IEEE 1394A interface and a PCI interface. The IEEE 1394A interface can support up to 5.3M events s^{-1} and the PCI interface up to 16.7M events s^{-1}.

The system has a coincidence timing resolution of 1.22 ns with each EPM's time to digital converter having a resolution of 312 ps. The coincidence timing and energy windows are selectable for each acquisition. Random coincidence events are measured using a delayed-window technique. Data are acquired in list mode and can be sorted into three-dimensional (3D) sinograms with various spans and maximum ring differences or into two-dimensional (2D) sinograms by single slice rebinning (SSRB) (Daube-Witherspoon and Muehllehner 1987).

The Inveon™ PET system in our laboratory is a stand-alone device. It can be operated in dedicated PET mode or, alternatively, it can be docked with the x-ray computed tomography (CT) system and operated in multi-modality mode. The CT system is not evaluated here. The CT gantry has been designed to incorporate a multi-headed single photon computed tomography (SPECT) system and the PET system. The Inveon™ PET system is also equipped with two rotating Co-57 point source for performing transmission-based attenuation correction. In Inveon™ Acquisition Software (IAS) version 1.2, transmission scanning is performed by continuously rotating one Co-57 source and translating the bed in a step-and-shoot motion. Alternatively, attenuation correction can be performed using the dock-able CT system.

Performance measurements

The NEMA NU 2-2007 standard for whole-body PET scanners (National Electrical Manufacturers Association 2007) with appropriately scaled phantoms was utilized to test the Inveon™ PET system. NEMA NU 2-2007 was developed to address the testing of scanners with intrinsic radiation in the crystals (Watson *et al* 2004). LSO contains 2.6% ^{176}Lu which decays by β-emission and a subsequent cascade of gamma and x-rays. The detection of a β- in one crystal and a single ^{176}Lu gamma ray (78% at 202 keV and 94% at 307 keV) in a second crystal results in an intrinsic true coincidence event. In addition, random coincidences occur when the annihilation photon from a true decay is detected in coincidence with either the β- or ^{176}Lu gamma ray. Consequently, the true and randoms intrinsic coincidences are indistinguishable from the true and random coincidences from the extrinsic radiation. This gives rise to the concept of a characteristic extrinsic activity threshold, a_{ref}, above which the singles rate from extrinsic radiation is greater than that from the intrinsic radiation (Watson *et al* 2004). Knowledge of the intrinsic coincidence event rate is important for accurate measurement of the scanner performance and it is also important for the selection of the energy window in imaging small animals at low activity levels (Goertzen *et al* 2007).

During the final preparation of this paper NEMA NU 4-2008, Performance Measurements of Small Animal Positron Emission Tomographs was released (National Electrical Manufacturers Association 2008).

Spatial resolution

To measure reconstructed spatial resolution, a 350 kBq (9.5 μCi) ^{22}Na point source, with a nominal diameter of 0.30 mm embedded in a 25 mm diameter by 6 mm thick acrylic disk (Isotope Products Laboratories, Valencia, CA), was scanned at radial offsets of 0, 1, 5, 10, 20, 30, 40 and 45 mm from the scanner axis. The point source was positioned at the axial center (position Z0) and at an axial offset of 1/4 of the axial FOV from the center of the axial FOV (position ZQ), and at each of these two locations the source was stepped by 0.2 mm in the axial direction. The duration of all acquisitions was 120 s and a minimum of 2 million true events were collected during each acquisition. An energy window of 350–650 keV and a coincidence timing window of 3.43 ns were used.

Data were acquired in list mode and sorted into 3D sinograms using the following scanner default parameters: span of 3 and a maximum ring difference of 79 for a maximum axial acceptance angle of 38.3°. The data were also sorted into 3D sinograms using a span of 3 and maximum ring differences of 49, 28, 13 and 1 (maximum axial acceptance angles of 26.1°, 15.6°, 7.4° and 0.6°, respectively). The sinograms were Fourier rebinned (FORE) (Defrise *et al* 1997) and images were reconstructed into a 256 × 256 matrix using 2D filtered backprojection (FBP) with a ramp filter (cutoff at Nyquist frequency) and zoom of 2. The reconstructed images had a pixel size of 0.194 mm and a slice thickness of 0.796 mm.

As specified by the NEMA NU 2-2007 standard, profiles with a width of approximately twice the FWHM were traced through the peak of the reconstructed point source in the tangential, radial and axial directions. In addition, thin one-pixel profiles through the peak of the reconstructed point source were also generated. In the axial direction, an oversampled profile was assembled by interleaving the profiles from the four stepped acquisitions. The FWHM and full width at tenth maximum (FWTM) of the profiles were calculated using linear interpolation between adjacent pixels at one-half and one-tenth the maximum count value; the maximum count value was calculated from a parabolic fit through the maximum and the two neighboring points. System resolution was reported as the average of resolutions measured at the axial center and 1/4 of the axial FOV. The volumetric resolution was calculated as the product of the tangential, radial and axial resolutions.

Sensitivity

The sensitivity of the scanner was measured using NEMA methodology in which acquisitions of a line source placed within successive layers of metal sleeves were performed. The NEMA PET sensitivity phantom (Data Spectrum Corp., Hillsborough, NC) used for these acquisitions comprised five concentric aluminum sleeves with a wall thickness of 2.5 mm and length of 700 mm. A plastic line source with a diameter of 2.0 mm was filled with 3.33 MBq (90 μCi) ^{18}F and threaded through the inner sleeve; the activity in this source was uniformly distributed over a length of 200 mm.

Successive measurements were acquired with up to five aluminum sleeves surrounding the line source for the phantom positioned in the center of the transaxial FOV and at a radial distance of 10 mm from the scanner axis. For each sleeve configuration, two energy windows (350–650 keV and 250–750 keV) and two coincidence timing windows (3.43 ns and 4.06 ns) were acquired at each radial location. The acquisition duration was 60 s and a minimum of 2 million true events were collected per acquisition.

Single slice rebinning was applied to the list-mode data to assign each oblique line of response (LOR) to the slice where the LOR crosses the scanner axis; the default maximum ring difference of 79 was used. True events were obtained by subtracting delayed events from the prompts prior to rebinning, and the system true event rate and the true event rate per slice were computed.

The true event rates for each acquisition were corrected for activity decay. The natural logarithm of the true count rate for each sleeve was plotted as a function of sleeve thickness and a linear equation was fit to the data. The count rate without attenuation (i.e. sleeve thickness of zero) is represented by the intercept of this equation, and the total system sensitivity is the count rate without attenuation divided by the activity in the line source. Correction factors to account for the beta decay branching ratio (96.7%) of ^{18}F and to include only the section of the line source within the axial FOV were applied to the measured line source activity. These corrections are not NEMA standard but were applied to be consistent with other performance papers. The sensitivity as a function of axial position was also generated using the true event rate per slice acquired for the source surrounded by the smallest diameter sleeve at the center of the transaxial FOV.

As stipulated by the NEMA standard, sensitivity was reported in units of cps kBq^{-1}. In addition, it is customary to report the peak system sensitivity for small animal scanners using a point source measurement. Therefore, the system (line source) sensitivity was converted to percent sensitivity of a point source at the center of the scanner using the relationship: point source sensitivity = 2 × line source sensitivity (Knoess *et al* 2003). The sensitivity for the two energy windows and coincidence timing window of 3.43 ns was also computed using SSRB histograms generated using maximum ring differences of 49, 28, 13 and 1.

Scatter fraction and count rate measurements

The scatter fraction and count rate measurements were performed using two different sized phantoms of design similar to the NEMA scatter phantom. Both phantoms were right, circular cylinders of polyethylene (density 0.96 g cm^{-3}) with a hole 3.2 mm in diameter located off axis and running parallel to the central axis of the cylinder. Plastic tubing representing a line source was inserted into the hole. The mouse-sized phantom was 25 mm in diameter and 70 mm long with the hole located at a radial distance of 10 mm from the central axis. The rat-sized phantom was 50 mm in diameter and 150 mm long with the hole located at a radial offset of 17.5 mm from the central axis. The volume of the line source was 0.28 mL and 0.54 mL for the mouse and rat-sized phantoms, respectively.

The line source was filled with 560 MBq (15.1 mCi) of ^{11}C and the activity distribution in the line source was the same length as the respective phantom. The phantom was centered in the transaxial and axial FOVs and positioned such that the line source was located away from the bed. List-mode data were collected using two energy windows (350–650 keV and 250–750 keV) and two coincidence timing windows (3.43 ns and 4.06 ns) in an interleaved manner for 60 s for 30 frames followed by 90 s for 20 frames. Single slice rebinning was applied to sort the list-mode data into a single sinogram for each slice; separate prompt and delayed event sinograms were generated.

The analysis of the count rate data was adapted from the NEMA NU 2-2007 methodology. To begin, prompt and delayed event sinograms were masked to a FOV of 25% greater than the phantom diameter: a 30 mm FOV for the mouse phantom and a 60 mm FOV for the rat phantom. Subsequently, the prompt sinogram was shifted such that the maximum activity in each projection was located in the central pixel. The same shift was applied to the corresponding projection in the delayed event sinogram. The total events ($C_{\mathrm{TOT},i,j}$) and random events ($C_{r,i,j}$) were calculated as the total counts within slice i of the masked prompt and delayed event sinograms of acquisition j. The random and scatter events for slice i of acquisition j ($C_{r+s,i,j}$) were computed as the sum of the counts outside a central 14 mm strip in the prompt sinogram plus a fraction of counts within this 14 mm strip, as stipulated by NEMA.

The true event rate for slice i of acquisition j was defined as $R_{t,i,j}=\frac{(C_{\mathrm{TOT},i,j}-C_{r+s,i,j})}{T_{\mathrm{acq},j}}$, where T_{acq} was the duration of acquisition j. The system true event rate $R_{t,j}$ was the sum of $R_{t,i,j}$ over all slices i. The random event rate for slice i of acquisition j is defined as $R_{r,i,j}=\frac{C_{r,i,j}}{T_{\mathrm{acq},j}}$ and the system random event rate $R_{r,j}$ was the sum of $R_{r,i,j}$ over all slices i. The scatter event rate for slice i of acquisition j was defined as $R_{s,i,j}=\frac{C_{r+s,i,j}-C_{r,i,j}}{T_{\mathrm{acq},j}}$ and the system scatter event rate $R_{s,j}$ was the sum of $R_{s,i,j}$ over all slices. The scatter fraction for slice i of acquisition j was calculated as $SF_{i,j}=\frac{C_{r+s,i,j}-C_{r,i,j}}{C_{\mathrm{TOT},i,j}-C_{r,i,j}}$ and the system scatter fraction was computed as $SF_j=\frac{\sum_i C_{r+s,i,j}-\sum_i C_{r,i,j}}{\sum_i C_{\mathrm{TOT},i,j}-\sum_i C_{r,i,j}}$. The characteristic extrinsic activity threshold (denoted as a_{ref}), above which the singles rate from extrinsic radiation is greater than that from the intrinsic radiation, was computed for all acquisitions. It is defined as the activity at which the singles rate is $2^* s_{\mathrm{int}}$, where s_{int} is the singles rate from the intrinsic raditation (Watson *et al* 2004). The scatter fraction was computed using the average of three measurements taken near a_{ref}.

The noise equivalent count rate for slice i of acquisition j was defined as $R_{\mathrm{NEC},i,j}=\frac{R_{t,i,j}^2}{R_{\mathrm{TOT},i,j}+kR_{r,i,j}}$ where $k = 0$ for noiseless estimate of random events (denoted as NECR 1R) and $k = 1$ for direct random event subtraction (denoted as NECR 2R). The system noise equivalent count rate $R_{\mathrm{NEC},j}$ is computed as the sum of $R_{\mathrm{NEC},i,j}$ over all slices i. The maximum system true event rate $R_{t,j}$ and maximum system noise equivalent count rate $R_{\mathrm{NEC},j}$ and the activity at these maximums were reported.

Corrections for count losses and randoms

The list-mode data acquired in the count rate measurements were used to measure the accuracy of the corrections for dead time losses and random events. 3D sinograms generated using a span of 3 and maximum ring difference of 79 were reconstructed using filtered backprojection into a 128 × 128 matrix with a FOV of 45 cm. FORE was applied to the 3D sinograms prior to filtered backprojection. Corrections for deadtime and randoms were applied; no corrections for attenuation or scatter were applied.

From the reconstructed images, the true event rate $R_{\mathrm{ROI},i,j}$ in the 45 mm FOV was computed for each slice i and each acquisition j. The extrapolated true event rate $R_{\mathrm{EXT},i,j}$ was computed by scaling the activity at each acquisition j by the ratio of $R_{\mathrm{ROI},i,j}$ to the activity at a low count frame, typically a frame with an activity of approximately 4 MBq. The relative true event rate error for slice i of acquisition j was computed as $\Delta r_{i,j}=100\left(\frac{R_{\mathrm{ROI},i,j}}{R_{\mathrm{EXT},i,j}}-1\right)\%$. The mean relative true event error across all slices was calculated for each acquisition, and the maximum absolute value of the mean bias was determined for those acquisitions with activity values at or below the activity at peak R_{NEC}.

Energy resolution

The energy resolution of the system was measured by using a ^{68}Ge cylindrical phantom with the system in detector calibration mode. Energy spectra were acquired for each crystal, and the energy resolution computed as the FWHM of the 511 keV photopeak divided by the peak energy value, expressed as a percent. The mean value of all crystal energy resolutions was reported.

Recovery coefficients

The recovery coefficient of an object is the ratio of the apparent activity concentration to the true activity concentration. The recovery coefficients for spheres of various diameters were measured; nine plastic spheres (Data Spectrum Corp., Hillsborough, NC) with inner diameters ranging from 3.95 to 24.8 mm (volumes of 0.031–8.0 mL) were filled with an ^{18}F activity concentration of 2.4 MBq mL^{-1} (64 μCi mL^{-1}) and imaged one at a time. For all acquisitions, an energy window of 350–650 keV and a coincidence timing window of 3.43 ns were used. The emission scan for the first sphere was performed for 600 s; the duration of subsequent emission scans for the other spheres was increased to account for activity decay. A transmission scan of 10 min was acquired for each sphere. The list-mode data were rebinned into sinograms of span 3 and ring difference 79. Images were reconstructed using FORE and 2D ordered subset expectation maximization (OSEM). Corrections for randoms, attenuation, scatter and deadtime were applied.

For each sphere, regions of interest containing those pixels with activity concentration greater than 50% of the maximum activity concentration were drawn on each transverse slice. The recovery coefficients were obtained by normalizing the mean activity concentration for a particular sphere to the greatest mean activity concentration in the group of spheres. The images

with and without attenuation correction were treated as separate groups in the calculation of recovery coefficients.

Derenzo phantom

A micro Derenzo phantom (Data Spectrum Corp., Hillsborough, NC) was imaged to evaluate system performance. This phantom has hollow channels of diameters 0.8, 1.0, 1.25, 1.5, 2.0 and 2.5 mm; the center-to-center spacing between adjacent channels is twice the diameter of a channel. The phantom was filled with 46 MBq (1.25 mCi) ^{18}F and a dynamic study of six 1 h frames was acquired. A 5 min transmission scan was acquired for attenuation correction purposes. The sinograms were reconstructed with FORE + 2D OSEM into a 128 × 128 matrix with a zoom of 2. Corrections for randoms, geometry, attenuation and scatter correction were applied. The reconstructed image had a voxel size of 0.41 × 0.41 × 0.80 mm^3.

Results

Spatial resolution

The tangential, radial and axial reconstructed spatial resolutions as a function of radial position are shown in figure 1(a). The spatial resolution at the center of the transaxial FOV was 1.56, 1.62 and 2.12 mm in the tangential, radial and axial directions, respectively. The volumetric resolution at the center was 5.36 μL. For a thin, one pixel profile, the spatial resolution was 1.32, 1.37 and 2.09 mm in the tangential, radial and axial directions, respectively. At a radial offset of 20 mm, the spatial resolution was 1.72, 2.41 and 2.50 mm in the tangential, radial and axial directions, respectively, and the volumetric resolution was 10.36 μL. The tangential resolution is uniform throughout the FOV; it remains below 1.8 mm up to a 30 mm radial offset. As expected, the depth of interaction effects causes a reduction in the radial resolution as the radial offset is increased.

The axial resolution as a function of radial position for a source at Z0 and ZQ are shown for various maximum ring differences (MRD) in figures 1(b) and (c), respectively. For all MRDs, the best axial resolution is obtained at the center of the transaxial FOV. For the MRD of 79 with a source at Z0, the axial resolution degrades as the radial offset increases to 5–10 mm, and then improves before becoming constant. As the MRD is reduced, the axial resolution improves and the change in resolution becomes more linear as a function of the offset. For the source at ZQ the axial resolution for MRD 79 is equal to MRD 49. The axial resolution for an MRD of 28 and 13 is independent of the axial position of the source.

Sensitivity

The total system sensitivities for each energy window and timing window are given in table 1. The total system sensitivity at the center was 36 cps kBq^{-1} and 51 cps kBq^{-1} for energy windows of 350–650 keV and 250–750 keV, respectively. The difference in the total system sensitivity for the 3.43 ns or 4.06 ns coincidence timing windows was negligible; this is expected as the activity of the line source is low and the randoms coincidence count rate is negligible. There was a slight increase in sensitivity as the source is moved 10 mm off axis. The axial slice sensitivity profiles for both energy windows and a coincidence timing window of 3.43 ns are shown in figure 2. The total system sensitivity for various maximum ring differences is given in table 2. As the maximum ring difference decreases, there are fewer LORs with a concomitant decrease in sensitivity.

Scatter fraction and count rate measurements

The system singles rate is plotted as a function of activity in figure 3(a); shown are the results for the mouse- and rat-sized phantoms and two energy windows. Since the singles rate is

independent of the coincidence timing window, only the 3.43 ns timing window is shown. A linear regression was fit to these data and the intercept represents the singles rate due to the intrinsic radiation in the LSO crystals, denoted as s_{int}. The intrinsic singles rate s_{int} is independent of the object size and it is greater for the wider 250–750 keV energy window because of the detection of the intrinsic true events from the 307 keV ^{176}Lu gamma ray. Figures 3(b) and (c) show the randoms-to-trues ratio (RTR) as a function of singles rate for the mouse- and rat-sized phantoms, respectively, for two energy and coincidence timing windows. The minimum RTR occurs at a singles rate $2^{*}s_{int}$ or characteristic extrinsic activity threshold a_{ref}; below this activity, the singles rate from the intrinsic radiation from the LSO crystals is greater than the singles rate from extrinsic radiation. Table 3 lists a_{ref} and s_{int} for the mouse- and rat-sized phantoms for each energy and coincidence timing window configuration. These calculated values for s_{int} agree with singles rates measured from a 12 h acquisition with no external radioactivity in the system. For each phantom, RTR is greater for the wider 250–750 keV energy window because of the detection of the 307 keV ^{176}Lu gamma ray. Consequently s_{int} (and a_{ref}) is greater which indicates the need for increased extrinsic activity to overcome the higher intrinsic singles rate. The RTR is also greater for the rat-sized phantom and for the 4.06 ns coincidence timing window because more random events are detected.

The true event count rates are plotted as a function of activity in figures 4(a) and (b). For the mouse-sized phantom (figure 4(a)), the maximum true count rate was 2460 kcps at an activity of 161 MBq for the 250–750 keV energy window. The maximum true count rate was 1900 kcps at an activity of 150 MBq for the 350–650 keV energy window. The coincidence timing window did not affect the true event count rate. For the rat-sized phantom (figure 4(b)), the maximum true count rate was 1320 kcps at an activity of 128 MBq for the 250–750 keV energy window. The maximum true count rate was 1020 kcps at an activity of 118 MBq for the 350–650 keV energy window. Again, the effect of the coincidence timing window on the true event count rate was negligible.

The Inveon™ PET system uses direct randoms subtraction to correct for random coincidences. Therefore, the NECR curves for noisy randoms estimate (NECR 2R) are plotted as a function of activity in figure 4(c) for the mouse phantom and in figure 4(d) for the rat phantom. The maximum NECR for noiseless and noisy randoms estimates and the activity at the maximum are listed in table 4. For the mouse-sized phantom (figure 4(c)), the maximum NECR 2R was 1801 kcps at an activity of 119 MBq for the 250–750 keV energy window and 3.43 coincidence timing window. Similarly, the maximum NECR 2R was 1475 kcps at 130 MBq for the 350–650 keV energy window and 3.43 coincidence timing window. For each energy window configuration, the maximum NECR was decreased by approximately 1% when using the wider 4.06 ns coincidence timing window, due to the fact that more random coincidence events are included in the prompt events.

For the rat-sized phantom, the maximum NECR 2R was 646 kcps at an activity of 81 MBq for the 250–750 keV energy window and 3.43 coincidence timing window (figure 3(d)). Similarly, the maximum NECR 2R was 583 kcps at 74 MBq for the 350–650 keV energy window and 3.43 coincidence timing window. For each energy window configuration, the maximum NECR was decreased by approximately 3% when using the wider 4.06 ns coincidence timing window.

The system scatter fractions as a function of activity for the mouse- and rat-sized phantoms are plotted in figure 5(a). For both phantoms, the scatter fraction is relatively stable as the activity in the scanner increases; the scatter fractions increase by 2% as the activity is increased to the activity at peak NECR. For the mouse phantom, the scatter fraction was 5.7% for the 350–650 keV energy window and 9.2% for the 250–750 keV energy window. Similarly, at low activities, for the rat phantom, the scatter fraction was 14.6% for the 350–650 keV energy window and 24.7% for the 250–750 keV energy window. At activities below a_{ref}, the presence

of the intrinsic true events from the 307 keV ^{176}Lu gamma ray is apparent in the 250–750 keV energy window. For each phantom and energy window, the scatter fractions are equivalent for the 3.43 and 4.06 ns coincidence timing windows.

The scatter fractions for the mouse- and rat-sized phantoms as a function of slice are shown in figure 5(b). For the mouse-sized phantom, the scatter fraction is shown for only those slices that contained the line source. The scatter fraction is stable across all slices for the 350–650 keV energy window (median 5.7%, range 5.1–6.1%), and for the 250–650 keV energy window, the scatter fraction increases and there is greater variation across slices (median 9.2%, range 8.4–10.1%). For the rat-sized phantom, the scatter fraction is 14.6% (range 12.2–15.8%) for the 350–650 keV energy window and increases with greater variability (median 25.3%, range 24.3–28.7%) for the 250–750 keV energy window.

Corrections for count losses and randoms

The mean relative true event rate errors for the mouse and rat phantom are plotted in figure 6. For the mouse-sized phantom at activities less than 60 MBq, there is 1.1–2.5% overestimation in the reconstructed true event rate for all configurations except the 250–750 keV, 3.43 ns configuration; for this configuration, there is an underestimation of the reconstructed true event rate for all activities. The maximum absolute value of the mean relative true event rate error is <5% up to the activity at which the maximum NECR is attained.

For the rat-sized phantom, there is an underestimation of the mean relative true event rate for all activities and for all acquisition configurations. The maximum absolute value of the mean relative true event rate error is <6.5% up to the activity at which the maximum NECR is attained.

Energy resolution

The mean energy resolution of the system for all crystals was 15.3 ± 1.5%. The median energy resolution was 15.1% with a range of 11.6–33.9%.

Recovery coefficients

The recovery coefficients are listed as a function of the inner diameter of the sphere in table 5. The data show the high-resolution characteristics of the scanner, as the recovery coefficient is greater than 0.85 for spheres with an internal diameter greater than 8 mm (volume 250 mm^3).

Micro Derenzo phantom

Reconstructed images of the micro Derenzo phantom for ^{18}F activity levels of 46 MBq, 22 MBq and 10 MBq are shown in figure 7. The 1.25 mm channels are clearly visible for all activity levels and the 1.0 mm channels can just be resolved. Moreover, all channels appear circular and do not exhibit radial elongation. This confirms that the scanner has excellent resolution across a wide range of activities.

Discussion

The performance specifications of the Inveon™ PET system demonstrate that it possesses high sensitivity, spatial resolution and count rate performance. The system has a transaxial FOV of 100 mm and an axial FOV of 127 mm, which makes it possible to image mice in one bed position. The Inveon™ PET system represents a redesign of the microPET Focus 120 small animal scanner (Laforest *et al* 2007, Kim *et al 2007*), which has a ring diameter of 150 mm and an axial extent of 76 mm. The Inveon™ PET scanner utilizes LSO crystals of similar dimensions as the Focus 120, but the crystals in the Inveon™ system are grouped into a 20 ×

20 array instead of a 12 × 12 array. Further, the Inveon™ system uses the new Quicksilver event processing architecture.

Spatial resolution is the most important design requirement for small animal PET tomographs. To accurately quantify the activity concentration in small structures, the resolution must be less than one-third of the object to be measured in order to avoid partial volume and spill-over effects. For the Inveon™ PET scanner the spatial resolution at the center of transaxial FOV was 1.56 mm, 1.62 mm and 2.12 mm in the tangential, radial and axial directions, respectively. For a one pixel thick profile, the spatial resolution at the center of the scanner was 1.32 mm, 1.37 mm and 2.09 mm in the tangential, radial, and axial directions, respectively. The volumetric resolution was 5.36 μL, 8.78 μL and 10.36 μL at the center and at radial distances of 10 and 20 mm, respectively. The transaxial spatial resolution of 1.36 mm at the center of the FOV is comparable to that of the microPET Focus 120 (Laforest *et al* 2007), which is expected since the size of the crystal is unchanged and the effect of non-collinearity for the different ring diameters is small.

The sensitivity of a PET tomograph is also important, as radiation dosimetry must be considered, especially for serial studies (Funk *et al* 2004), and as there is a limit to the volume of tracer that can be injected (Hume *et al* 1998). High sensitivity is also required for the acquisition of low noise static or dynamic images in as short a time as possible. The line source sensitivity of the scanner was 36.2 cps kBq^{-1} (7.2% absolute sensitivity with a point source) for an energy window of 350–650 keV and a coincidence timing window of 3.4 ns. As a comparison the microPET Focus 120 had a sensitivity of 3.8–4.4% for a similar energy window and a timing window of 6 ns (Laforest *et al* 2007, Kim *et al* 2007). The increase in sensitivity with the Inveon™ system can be attributed to the greater solid angle created from the larger axial FOV.

With a maximum ring difference of 79 the Inveon™ system has a maximum axial acceptance angle of 38.3°. At this large acceptance angle, the axial resolution will deteriorate at large radii because of a parallax effect due to the crystal penetration in the axial direction and because of a breakdown of the FORE (Matej *et al* 1998). However, in Siemens Inveon™ Acquisition Software version 1.2, an equal weight is applied to all oblique LORs during Fourier rebinning, and a reduced number of oblique LORs are used when collapsing the oblique LORs to the central plane defined by the ring difference. Therefore, highly oblique LORs are not used in the image reconstruction, and, as a result, the axial resolution is relatively uniform and does not deteriorate as the radial offset is increased. However, for the maximum ring difference of 79 the resolution is nonstationary in the axial plane for the same radial offset, and there is an effective loss in sensitivity that is not measured in the NEMA sinogram-based sensitivity metric.

If axial resolution is important for a particular study, then the maximum ring difference can be reduced. For example, a maximum ring difference of 28 will improve axial resolution by 0.1–0.4 mm, especially at smaller radial offsets, but this reduction in ring difference will subsequently reduce the sensitivity by 36%.

The count rate metrics demonstrate that the Inveon™ system with the Quicksilver event processing architecture has a high count rate capability. For a 350–650 keV energy window, the system has a peak true count rate of 1900 kcps at an activity of 150 MBq for a mouse phantom and 1020 kcps at an activity of 118 MBq for a rat phantom. With the same energy window and a 3.43 ns coincidence timing window, the peak NECR 2R was 1475 kcps at an activity of 130 MBq for a mouse-sized phantom and 583 kcps at an activity of 74 MBq for a rat-sized phantom. While the activity of the peak count rate exceeds the activity that would typically be administered in a small animal cancer model or in a gene expression experiment,

it is important to have high count rate capability for dynamic cardiac studies. The NECR was decreased by approximately 1–3% when the wider 4.06 ns coincidence timing window was used as a greater number of random events are detected. The NECR for the mouse phantom is greater than the NECR for the rat phantom because there is less attenuation of the true events and less scatter and random events. In addition, the NECR for the mouse phantom peaks at a greater activity than the NECR for the rat phantom since the true events decrease more rapidly than the random events as the object size increases (Watson *et al* 2005). The characteristic extrinsic activity threshold a_{ref} suggests maintaining the activity above 0.3–0.4 MBq (11–15 μCi) in order to minimize the affect of the intrinsic coincidence events. In addition, the intrinsic coincidence events were lower for the 350–650 keV energy window as the 307 keV ^{176}Lu gamma ray was not detected; this suggests the use of the narrow energy window when imaging weak source distributions (Goertzen *et al* 2007). The reconstructed images show that corrections for deadtime and random events were effective; the quantitative accuracy was <5% and <6.5% for the mouse- and rat-sized phantoms, respectively, up to the activity at maximum NECR.

The scatter fraction of the Inveon™ PET scanner at low activities and a 350–650 keV energy window was 5.7% for the mouse phantom and 14.6% for the rat phantom. The scatter fraction was increased nearly twofold for both phantoms when a 250–750 keV energy window was employed. The scatter fraction for the Inveon™ is lower than that of the Focus 120 because of the improved energy resolution of the Inveon™: 15.3% for the Inveon™ versus 18.3% for the Focus 120 (Kim *et al* 2007). The scatter fraction also remained stable as the activity in the scanner increased.

The calculation of the scatter fraction will affect the computation of the NECR. The NECR for acquisition *j* can also be expressed as $R_{\text{NEC},j}=\frac{R_{T,j}^2(1-SF)^2}{R_{T,j}+k\alpha R_{r,j}}$ (Strother *et al* 1990)where R_T is the true plus scatter events rate (i.e. $R_{t+s,j}$, calculated as a difference of the prompt rate and the delayed event rate) for the entire FOV, *SF* is the *fixed* scatter fraction and α is the fraction of the object in the FOV. Using this formula for the mouse-sized phantom with an energy window of 250–750 keV, a coincidence timing window of 4.06 ns and α of 0.255, the peak NECR 1R was 2261 kcps for a scatter fraction of 9.4% (minimum value) and 2162 kcps for a scatter fraction of 11.4% (value at peak NECR). As a comparison, Laforest found the peak NECR 1R to be 809 kcps at an activity of 88 MBq for the mouse-sized phantom (Laforest *et al* 2007) with a 6 ns coincidence timing window. The higher NECR value for the Inveon™ can be attributed to the higher count rate capability and lower scatter fraction, and, in this comparison, the narrower 4.06 ns coincidence timing window.

Conclusion

The performance measurements indicate that the Inveon™ PET scanner is a high-resolution tomograph with excellent sensitivity and scatter fraction that is capable of imaging at a high count rate. The acquisition parameters of energy and coincidence timing windows and the histogramming parameter of maximum ring difference are configurable and should be selected based on the imaging task.

Acknowledgments

This work was supported in part by a research grant from Siemens Medical Solutions USA, Inc.

References

Atkins, BE.; Pressley, DR.; Lenox, MW.; Swann, BK.; Newport, DF.; Siegel, SB. In: Phlips, Bernard, editor. A data acquisition, event processing and coincidence determination module for a distributed

parallel processing architecture for PET and SPECT; 2006 IEEE Nuclear Science Symp. and Conf. Record [book on CD-ROM]; San Diego, CA: Institute of Electrical and Electronics Engineers; 2006.

Cherry SR. The 2006 Henry Wagner Lecture: of mice and men (and positrons)—advances in PET imaging technology. J Nucl Med 2006;47:1735–45. [PubMed: 17079804]

Cherry SR, et al. MicroPET: a high resolution PET scanner for imaging small animals. IEEE Trans Nucl Sci 1997;44:1161–6.

Daube-Witherspoon ME, Muehllehner G. Treatment of axial data in three-dimensional PET. J Nucl Med 1987;28:1717–24. [PubMed: 3499493]

Defrise M, Kinahan PE, Townsend DW, Michel C, Sibomana M, Newport DF. Exact and approximate rebinning algorithms for 3-D PET data. IEEE Trans Med Imaging 1997;16:145–58. [PubMed: 9101324]

Funk TM, Sun M, Hasegawa BH. Radiation dose estimate in small animal SPECT and PET. Med Phys 2004;31:2680–6. [PubMed: 15487751]

Goertzen AL, Suk JY, Thompson CJ. Imaging of weak-source distributions in LSO-based small-animal PET scanners. J Nucl Med 2007;48:1692–8. [PubMed: 17873140]

Herschman HR. Micro-PET imaging and small animal models of disease. Curr Opin Immunol 2003;15:378–84. [PubMed: 12900267]

Huisman MC, Reder S, Weber AW, Ziegler SI, Schwaiger M. Performance evaluation of the Philips MOSAIC small animal PET scanner. Eur J Nucl Med Mol Imaging 2007;34:532–40. [PubMed: 17119959]

Hume SP, Brown DJ, Asworth S, Hirani E, Luthra SK, Lammertsma AA. *In vivo* saturation kinetics of two dopamine transporter probes measured using a small animal scanner. J Neurosci Methods 1997;76:45–51. [PubMed: 9334938]

Hume SP, Gunn RN, Jones T. Pharmacological constraints associated with positron emission tomographic scanning of small laboratory animals. Eur J Nucl Med 1998;25:173–6. [PubMed: 9473266]

Jeavons AP, Chandler RA, Dettmar CAR. A 3D HIDAC PET camera with sub-millimetre resolution for imaging small animals. IEEE Trans Nucl Sci 1999;46:468–73.

Kim JS, Lee JS, Im KC, Kim SJ, Kim SY, Lee DS, Moon DH. Performance measurement of the microPET Focus 120 scanner. J Nucl Med 2007;48:1527–35. [PubMed: 17704248]

Knoess C, et al. Performance evaluation of the microPET R4 PET scanner for rodents. Eur J Nucl Med Mol Imaging 2003;30:737–47. [PubMed: 12536244]

Laforest R, Longford D, Siegel S, Newport DF, Yap J. Performance evaluation of the microPET-Focus-F120. IEEE Trans Nucl Sci 2007;54:42–9.

Lecomte R, Cadorette J, Richard P, Rodrigue S, Rouleau D. Design and engineering aspects of a high resolution positron tomography for small animal imaging. IEEE Trans Nucl Sci 1994;41:1446–52.

Matej S, Karp JS, Lewitt RM, Becher AJ. Performance of the Fourier rebinning algorithm for PET with large acceptance angles. Phys Med Biol 1998;43:787–95. [PubMed: 9572504]

McFarland, AR.; Newport, DF.; Atkins, BE.; Pressley, DR.; Siegel, SB.; Lenox, MW. A compact PCI based event routing subsystem for PET and SPECT data acquisition. In: Phlips, Bernard, editor. 2006 IEEE Nuclear Science Symp. and Conf. Record [book on CD-ROM]; San Diego, CA: Institute of Electrical and Electronics Engineers; 2006.

National Electrical Manufacturers Association. NEMA Standards Publication NU 2-2007. Rosslyn, VA: National Electrical Manufacturers Association; 2007. Performance measurements of positron emission tomographs.

National Electrical Manufacturers Association. NEMA Standards Publication NU 4-2008. Rosslyn, VA: National Electrical Manufacturers Association; 2008. Performance measurements of small animal positron emission tomographs.

Newport, DF.; Siegel, SB.; Swann, BK.; Atkins, BE.; McFarland, AR.; Pressley, DR.; Lenox, MW.; Nutt, RE. In: Phlips, Bernard, editor. Quicksilver: a flexible, extensible and high-speed architecture for multi-modality imaging; 2006 IEEE Nuclear Science Symp. and Conf. Record [book on CD-ROM]; San Diego, CA: Institute of Electrical and Electronics Engineers; 2006.

Strother SC, Casey ME, Hoffman EJ. Measuring PET scanner sensitivity: relating count rates to image signal-to-noise ratios using noise equivalent counts. IEEE Trans Nucl Sci 1990;37:783–8.

Tai YC, Ruangma A, Rowland D, Siegel S, Newport DF, Chow RL, Laforest R. Performance evaluation of the microPET Focus: a third-generation microPET scanner dedicated to animal imaging. J Nucl Med 2005;46:455–63. [PubMed: 15750159]

Tatsumi M, Nakamoto Y, Traughber B, Marshall LT, Geschwind JFH, Wahl RL. Initial experience in small animal tumor imaging with a clinical positron emission tomography/computed tomography scanner using 2-[F-18]fluoro-2-deoxy-d-glucose. Cancer Res 2003;63:6252–7. [PubMed: 14559811]

Watson CC, Casey ME, Ericksson L, Mulnix T, Adams D, Bendriem B. NEMA NU 2 performance tests for scanners with intrinsic radioactivity. J Nucl Med 2004;45:822–6. [PubMed: 15136632]

Watson CC, et al. Optimizing injected dose in clinical PET by accurately modeling the count-rate response functions specific to individual patient scans. J Nucl Med 2005;46:1825–34. [PubMed: 16269596]

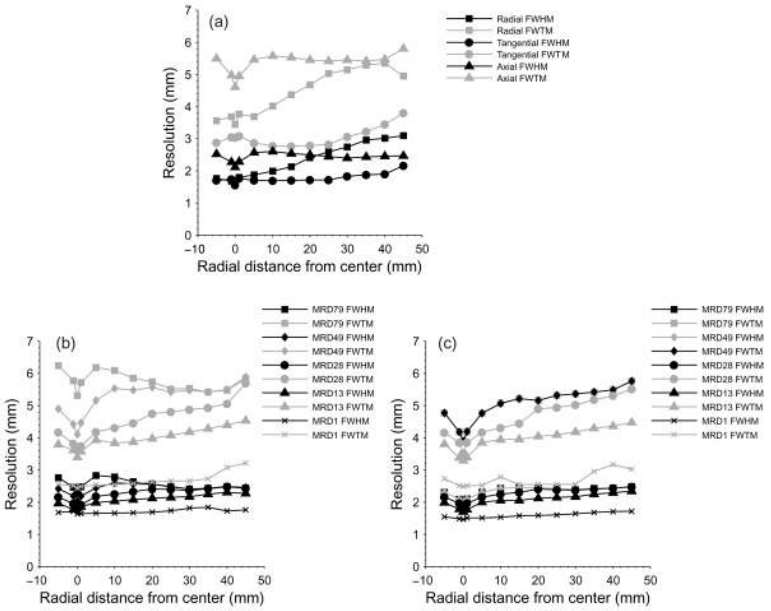

Figure 1.

Reconstructed spatial resolution measured with a ^{22}Na point source. (a) The radial, tangential and axial FWHM and FWTM resolutions. (b) Axial resolution as a function of the radial distance for various maximum ring differences (MRD) for a source located at the center of the axial FOV (Z0). (c) Axial resolution as a function of the radial distance for various MRDs for a source located at one-quarter axial FOV from the axial center (ZQ). The axial resolution plotted in (a) is the average of the axial resolutions in (b) and (c) for a MRD of 79. In (c), the symbols for the FWHM and FWTM axial resolution for a MRD of 49 are gray and black, respectively, so they can be differentiated from the resolutions for a MRD of 79.

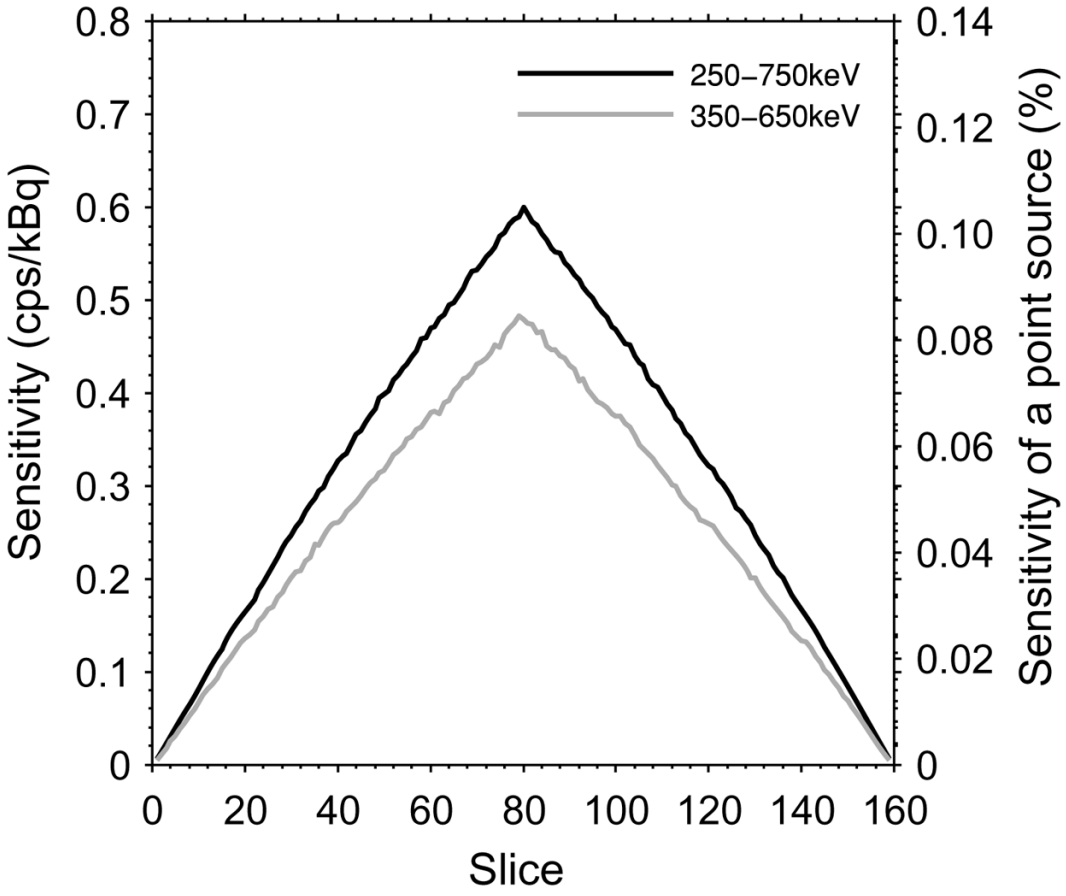

Figure 2.
System sensitivity as a function of slice within the scanner for energy windows of 350–650 keV and 250–750 keV and a coincidence timing window of 3.43 ns.

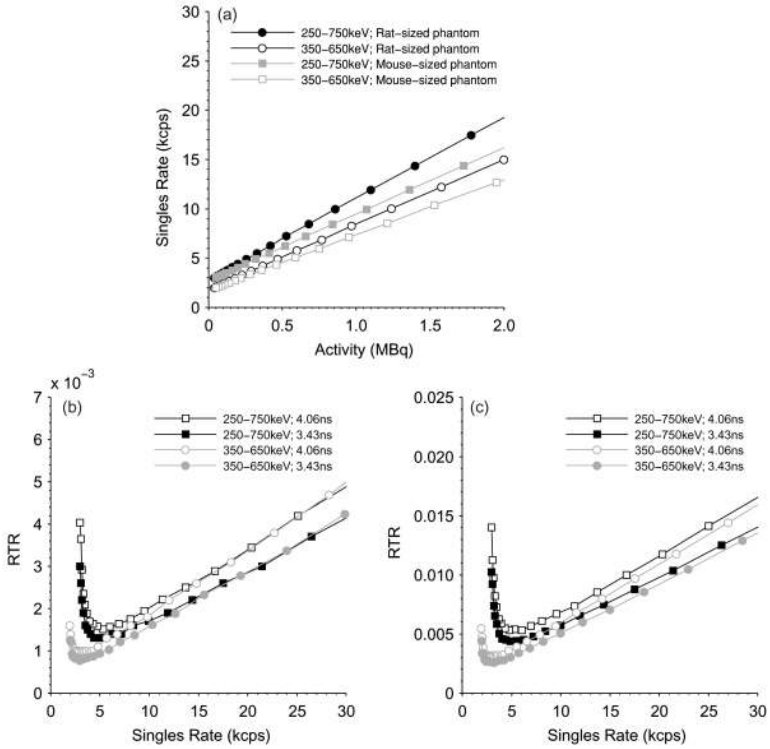

Figure 3.

(a) Singles rates as a function of activity for the mouse- and rat-sized phantoms. RTR as a function of singles rate for the (b) mouse- and (c) rat-sized phantoms for different configurations of energy and coincidence timing windows.

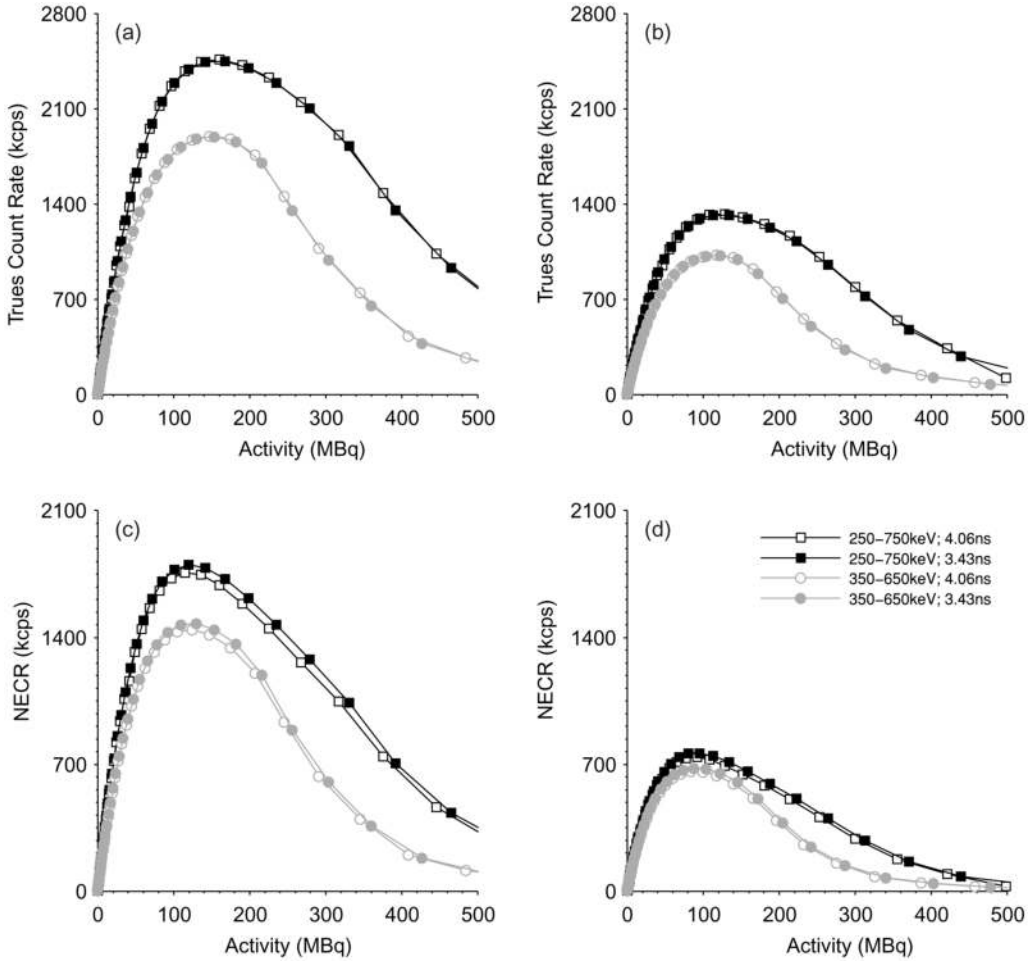

Figure 4.

True coincidence count rate for the (a) mouse- and (b) rat-sized phantoms. NECR 2R calculated using a noisy estimate of random coincidence events for the (c) mouse- and (d) rat-sized phantoms. Shown in all graphs are the results for different configurations of energy and coincidence timing windows.

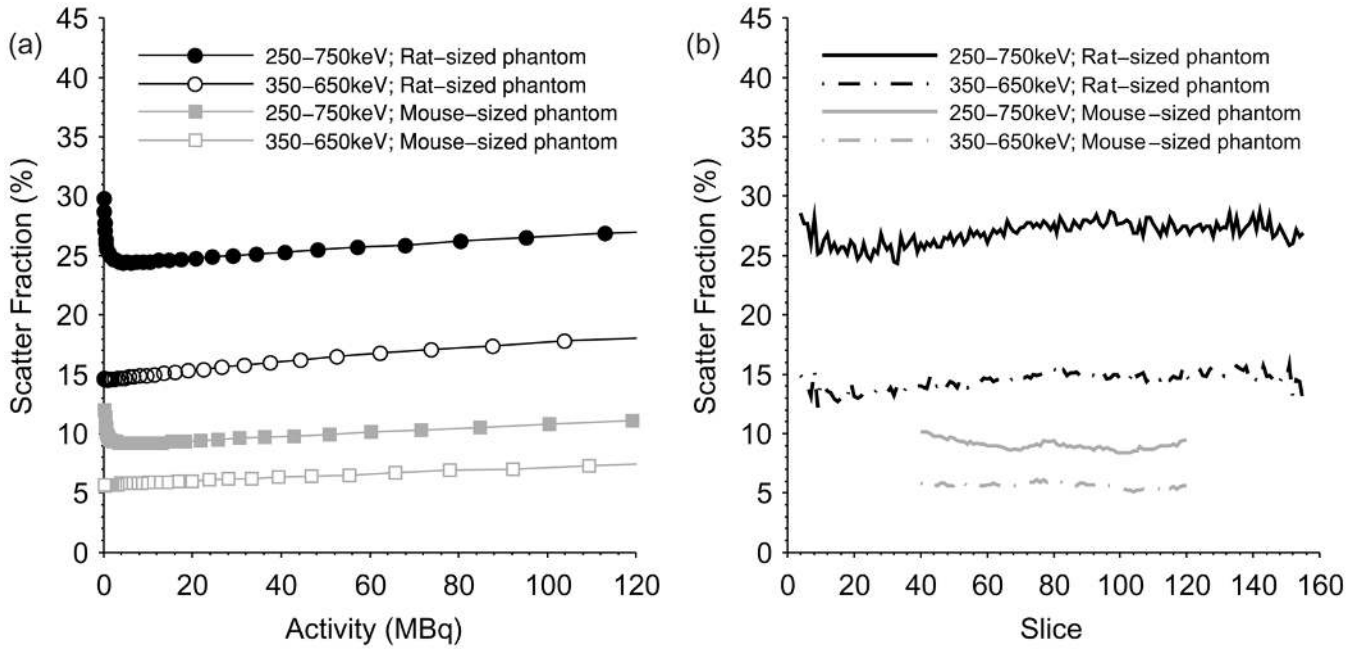

Figure 5.
(a) System scatter fractions as a function of activity for the mouse- and rat-sized phantoms. (b) Scatter fractions as a function of slice for the mouse- and rat-sized phantoms. For both graphs, the results for energy windows of 250–750 keV and 350–650 keV are shown.

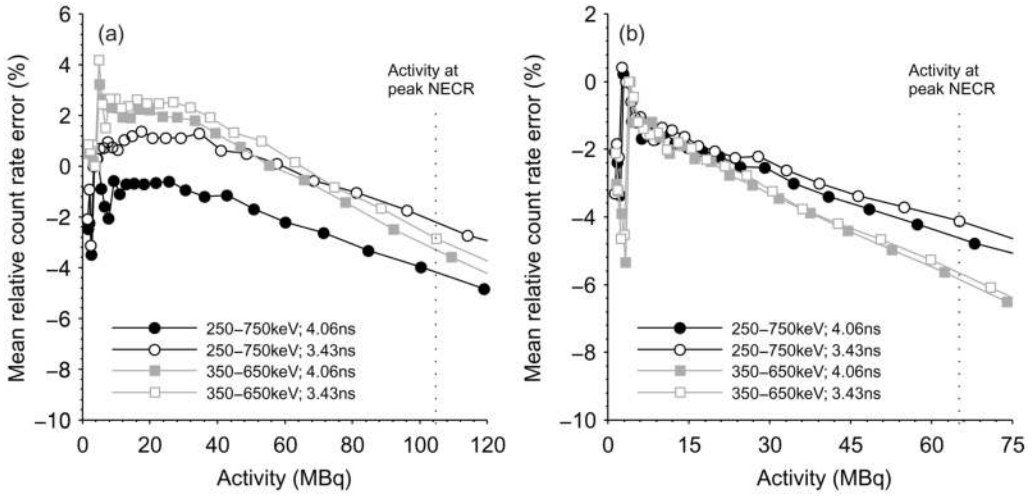

Figure 6.
Mean relative true event rate errors in the reconstructed images for the (a) mouse- and (b) rat-sized phantoms for different configurations of energy and coincidence timing windows.

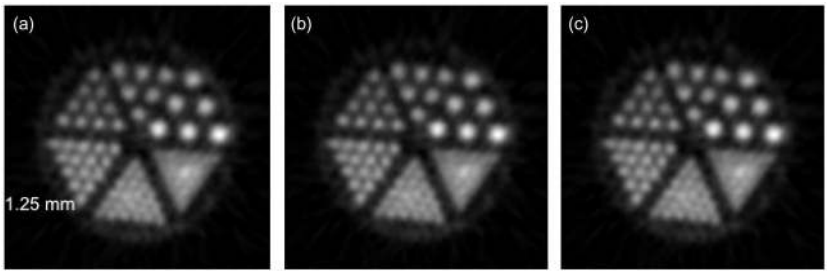

Figure 7.
Reconstructed images of the micro Derenzo phantom for activity levels of (a) 46 MBq, (b) 22 MBq and (c) 10 MBq. The hollow channels have diameters of 0.8, 1.0, 1.25, 1.5, 2.0 and 2.5 mm. The window level is set to the maximum intensity in each image. A broken channel caused a hot spot in the 0.8 mm sector.

Table 1

Total system sensitivity as a function of energy window and timing window for a line source at the center and at a 10 mm radial offset. The peak sensitivity for a centered point source expressed as a percent is given in parentheses.

	Timing window	
Energy window	**3.43 ns**	**4.06 ns**
Center		
350–650 keV	36.2[a] (7.2%)	36.5 (7.3%)
250–750 keV	51.1 (10.2%)	51.3 (10.3%)
10 mm radial offset		
350–650 keV	36.9 (7.4%)	36.5 (7.3%)
250–750 keV	53.4 (10.7%)	53.6 (10.7%)

[a] Total system sensitivity in cps kBq^{-1}.

Table 2

Total system sensitivity as a function of maximum ring difference for a line source at the center of the transaxial FOV. The timing window was 3.43 ns.

Maximum ring Difference	Energy window	
	350–650 keV	250–750 keV
79	36.2[a]	51.1
49	32.9	46.0
28	23.1	32.2
13	12.3	17.2
1	1.5	2.1

[a] Total system sensitivity in cps kBq^{-1}.

Table 3

The intrinsic singles rate s_{ref} and the characteristic activity a_{ref} for the mouse- and rat-sized phantoms for different configurations of energy and coincidence timing windows.

	Energy window 250–7.50 keV		Energy window 350–650 keV	
	s_{int}	a_{ref}	s_{int}	a_{ref}
Mouse-sized phantom				
3.43 ns	2.70[a]	0.40[b]	1.71	0.30
4.06 ns	2.69	0.40	1.71	0.30
Rat-sized phantom				
3.43 ns	2.73	0.33	1.73	0.26
4.06 ns	2.73	0.33	1.73	0.27

[a] s_{ref} in units of kcps.

[b] a_{ref} in units of MBq.

Table 4

The maximum NECR rate for noiseless (NECR 1R) and noisy (NECR 2R) randoms estimates and the activity at the maximum NECR for the different configurations of energy and coincidence timing windows.

	NECR 1R		NECR 2R	
	Maximum (kcps)	**Activity (MBq)**	**Maximum (kcps)**	**Activity (MBq)**
Mouse phantom				
350–650 keV; 3.43 ns	1597	130	1475	130
350–650 keV; 4.06 ns	1574	124	1441	124
250–750 keV; 3.43 ns	1959	141	1801	119
250–750 keV; 4.06 ns	1935	135	1758	114
Rat phantom				
350–650 keV; 3.43 ns	679	88	583	74
350–650 keV; 4.06 ns	660	84	556	71
250–750 keV; 3.43 ns	761	96	646	81
250–750 keV; 4.06 ns	739	92	616	77

Table 5

Recovery coefficients as a function of the inner diameter of the sphere.

Sphere diameter (mm)	Recovery coefficient
3.95	0.50
4.95	0.60
6.23	0.74
7.86	0.87
9.89	0.96
12.43	0.99
15.43	0.99
19.79	1.00
24.82	1.00